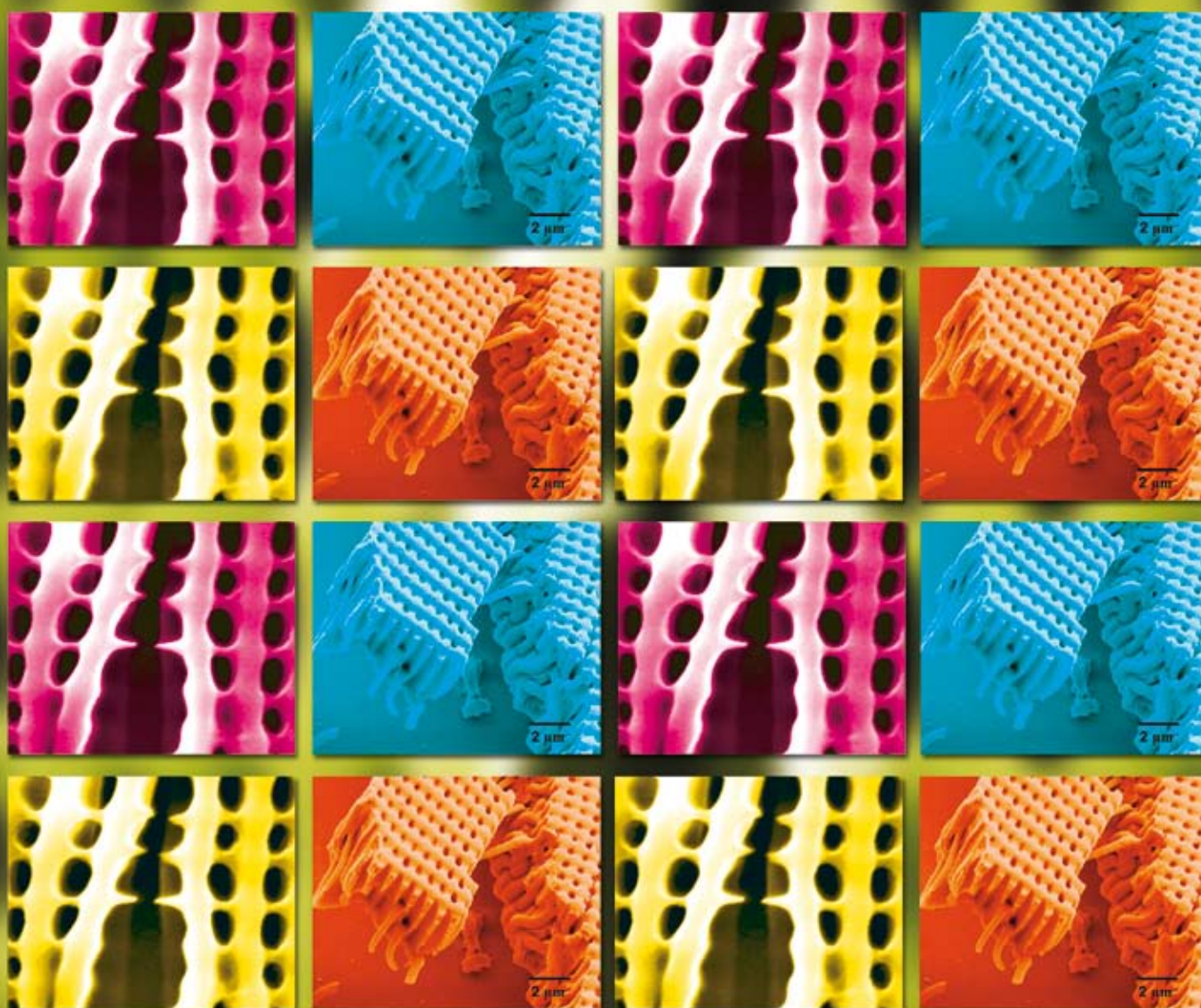


PCCP

Physical Chemistry Chemical Physics

www.rsc.org/pccp

Volume 10 | Number 28 | 28 July 2008 | Pages 4069–4200



ISSN 1463-9076

COVER ARTICLE

Tsukruk *et al.*
Mechanical properties of composite
polymer microstructures fabricated by
interference lithography

COMMUNICATION

Novoa *et al.*
[Cyanil]₂²⁻ dimers possess long,
two-electron ten-center (2e⁻/10c)
multicenter bonding

Mechanical properties of composite polymer microstructures fabricated by interference lithography

Srikanth Singamaneni,^{ab} Sehoon Chang,^{ab} Ji-Hyun Jang,^c Whitney Davis,^a Edwin L. Thomas^{*c} and Vladimir V. Tsukruk^{*ab}

Received 21st December 2007, Accepted 17th April 2008

First published as an Advance Article on the web 27th May 2008

DOI: 10.1039/b719709h

We demonstrate that organized, porous, polymer microstructures with continuous open nanoscale pores and a sub-micron spacing obtained *via* interference lithography can be successfully utilized in a non-traditional field of ordered polymer microcomposites. The examples presented here include porous matrices for the fabrication of binary, glassy-rubbery microcomposites with intriguing mechanical properties with large energy dissipation and lattice-controlled fracturing.

1. Introduction

Modern applications involving microfabricated structures and microdevices based upon polymeric materials call for sophisticated engineered surfaces and interfaces tailored to control elasticity, plasticity, adhesion, friction, chemical, and thermal properties. Specific examples of such applications include components for integrated photonic circuits, separation and chemical filtration, biological tissue scaffolding, biointerfaces and biosensors, environmental monitoring, microfluidic circuits, and MEMS-based sensors and actuators.^{1–11} Various sophisticated MEMS-based microdevices have already been fabricated from polymeric materials.¹² These include microgears, microcoils and pumps,^{13,14} microvalves and grippers,¹⁵ microchannels and high-aspect ratio beams,^{16–18} haircells,¹⁹ microcantilevers, and tribological coatings.^{20,21} A common approach for the fabrication of polymeric MEMS devices is the application of photolithographic techniques using epoxy-

based reactive materials such as SU8, a common negative photoresist.¹² On the other hand, soft lithography encompasses other approaches, including microcontact printing, capillary transfer lithography, imprint lithography, and edge lithography, to name a few.^{22–24}

Polymer/air (porous) structures, in which both phases are bi-continuous in three dimensions, exhibit large specific surface areas in conjunction with the controlled hierarchical porous network. This combination provides a unique platform for designing microstructured materials with interesting transport and adsorption properties. In addition to the steric effects imposed by the porous structure, chemical modification of the porous materials enables tailoring of the surface chemistry and polarity, which provides additional functionality. Porous materials find numerous applications in the field of life sciences, such as cell culture substrates for cell adhesion, biomaterials as tissue engineering scaffolds with biocompatible and biodegradable properties, cell patterning, and protein microarrays.^{25,26}

Dissipation and absorption of mechanical energy within highly porous microcomposite structures is another intriguing topic critical for some MEMS applications where high mechanical loads are involved. However, most of materials

^a School of Materials Science and Engineering, Georgia Institute of Technology, Atlanta, GA, USA. E-mail: vladimir@mse.gatech.edu

^b School of Polymer, Textile and Fiber Engineering, Georgia Institute of Technology, Atlanta, GA, USA

^c Department of Materials Science and Engineering, Massachusetts Institute of Technology, Cambridge, MA, USA. E-mail: elt@mit.edu



Srikanth Singamaneni is currently pursuing his PhD in Polymer Materials Science and Engineering at Georgia Institute of Technology. He has co-authored 30 refereed articles in archival journals and made presentations at national conferences. His current scientific interests include the fabrication of organic and inorganic nanostructured materials for ad-

vanced physical and chemical sensors, and interaction of electromagnetic radiation with metal nanostructures.



Vladimir V. Tsukruk holds a joint appointment as a Professor at the School of Materials Science and Engineering and School of Polymer, Fiber, and Textile Engineering, Georgia Institute of Technology. He has co-authored 250+ articles, 19 reviews, one book, co-edited three volumes, and holds four patents. His research activities are in the fields of surfaces/interfaces, molecular assembly, nano- and bioinspired materi-

als. He serves on the editorial advisory boards of *Polymer* and *Curr. Chem. Biology*.

suggested and discussed to date for such applications are either microscopic foams with random combination of open/close porous interior or macroscopic organized structures (such as civil engineering truss frames). Only a few examples of microscopic *organized porous structures* have been reported to date. Although foam-like structures can be exploited for lightweight designs with microscopic porous morphology, they exhibit much lower strengths and their high “polydispersity” leads to variation in the local physical properties on a microscopic scale.²⁷

Trusses are well known, highly organized 2D and 3D lightweight structural constructions composed of struts (beams) and nodes (joints) with excellent mechanical properties. They are widely used in civil engineering but rarely considered as examples for polymer microstructures. Recently, several miniature truss structures (with mm to cm dimensions) have been designed, fabricated, and tested.^{28,29} Outstanding specific mechanical properties are predicted for these structures. The design for ultimate stiff and lightweight truss structures should provide conditions such that the beams are under compression or tension (stretching) while avoiding bending.³⁰ Furthermore, the open architecture allows for potential beam and wall modification, as well as added functionality since the high surface area ($>100 \text{ m}^2 \text{ g}^{-1}$) allows for thermal cooling *via* a continuous fluidic phase or as a thermal barrier using evacuated pores.^{31,32} The design consideration includes specific application of the final structure since the mechanical properties exhibit a trade-off to a certain degree. Hence, for load bearing applications, the yield strain, yield stress, and creep properties of the structure have to be optimized.²⁷ For example, the materials for automotive applications need to be designed to withstand a strain rate of 40 s^{-1} , while those designed for ballistic protection are to be designed for strain rate of $\sim 2000 \text{ s}^{-1}$.

For some mechanical applications, pyramidal architectures have been predicted to be comparable or better than the benchmark honeycomb panels, but with potential for much lower density.³³ They are fully triangulated and show stretch-dominated properties. Kagome lattices, the name derived from Japanese weaves, are more efficient, offering the lowest mass-to-stiffness ratio.³⁴ Kagome and tetragonal microtruss structures are suggested as the most efficient designs with maximum stiffness and load limit achieved in combination with extreme lightweight properties. The minimum node connectivity for a class of lattice structured materials to be stretch-dominated is six for 2D and twelve for 3D.²⁷ The fabrication of conventional truss structures is usually a cumbersome routine, requiring a step-by-step assembly of numerous elements. Moreover, this process cannot be scaled down easily from common meter or sub-meter dimensions of panels and sub-meter or millimeter dimensions of beams to form truly microstructural architectures.

The fabrication of micro- and nanoporous materials from a variety of organic and inorganic materials has been developed by utilizing numerous bottom-up and top-down methods. Template-assisted fabrication is one of the most popular methods, where the porous structure is employed to obtain a negative replica of a second desired material. In this routine, porous templates have been achieved by the self assembly of

monodisperse submicron colloidal particles (*e.g.* silica or polymer particles) under carefully controlled processes such as sedimentation, centrifugation, filtration, dip coating, or slit filling.^{1,35,36} Subsequent infiltration and solidification of the second material (*e.g.* polymerizing the infiltrated monomer), followed by the removal of the template (colloidal crystal) by the dissolution of the particles (*e.g.* HF etch of SiO_2 colloidal spheres), leaves behind a highly porous polymeric structure. This simple technique, which relies on the foundations of colloidal crystallization, has been extended to achieve binary and ternary super lattices (particles of different sizes) by exploiting electrostatic interaction between oppositely charged particles.^{37,38}

The other important class of templates is the natural biological materials with complex periodicities which enable the fabrication of porous structures with complex ordering. Bacterial threads, echinoid skeletal plates, eggshell membranes, insect wings, pollengrains, plant leaves, and wood have been employed as biological templates.^{39–42} Other approaches such as breath figure templating,⁴³ dewetting of multilayered films²⁶ and selective etching of block copolymers⁴⁴ have achieved ordered porous structures. However, these methods suffer from limited range of available structural geometries and long time requirements to achieve templates with long range periodic structures. Most of the techniques discussed so far have a high density of undesired defects as well.

Multiple laser beam interference lithography (IL) is a facile technique for realizing uniform periodic polymeric structures over relatively large areas. It has been drawing increased attention over the past years.⁴⁵ The interference pattern is essentially a periodic light intensity distribution in one, two or three dimensions depending on the number of light beams interfering. A photocurable polymer (photoresist) exposed to the variable light intensity undergoes chemical crosslinking proportional to the local light intensity. Subsequent dissolution of the modified or unmodified portions results in a complex periodic polymeric structure replicating the original interference pattern. The technique offers fine control over the size and shape of the periodic structures, enabling the realization of much broader geometries than colloidal or block copolymer assembly can offer.^{46–49}

The interference of multiple laser beams was initially employed to write simple one-dimensional hologram gratings⁵⁰ and was later developed as a lithographic technique to create three-dimensional (3D) periodic polymeric structures⁵¹ for their application as photonic structures. Depending upon wavelength, geometry, and processing conditions, a variety of microporous polymer structures can be generated with a typical spacing in the range of 600 nm–1.3 μm , pore dimensions from 100 to 800 nm, strut diameters from 100 to 600 nm, and with the overall porosity ranging from 20 to 60%.^{52,53} Recently, we have demonstrated that the geometry and hence the phononic band gap of organized porous PDMS structures obtained through replication of original SU8 structure can be mechanically tuned.⁵⁴

The porous architectures with different lattice symmetries might serve as advanced mechanical structures, while their open porous design provides lightweight properties. For

demanding mechanical applications, the key is to select appropriate polymeric materials to create a “skeleton” network with proper 3D geometry for desired mechanical stress distribution. Very recently, interesting deformational behavior associated with buckling instabilities has been observed in 2D periodic elastomeric structures subjected to compressive stresses.⁵⁵ Understanding the elastic and plastic responses as well as the ultimate fracture behavior of the 3D microframes all become paramount. However, despite the recent spur of activities, the advantages of creating sophisticated 2D and 3D periodic microstructures with open, bicontinuous, porous network architectures as organized microcomposites with unique mechanical properties have not been realized.

This paper presents our results and ideas for exploiting organized microporous polymeric structures, obtained by interference lithography, as highly structured binary microcomposites. We demonstrate the ordered single and bi-component microstructures with a high degree of control over the microscopic organization of the polymeric phases and the mechanical properties of these structures. The microscopic and macroscopic mechanical (elastic and plastic) properties of these structures are discussed here in the relation to their organization. We also demonstrate the possibility of employing the organized microporous structures as masters in soft lithography, enabling the faithful replication of the complex topographical features with polymers using capillary transfer lithography. A recent review on the application of interference lithography for the fabrication of porous microstructures can

serve as an excellent introduction to the subject and is recommended to be read before this article.⁵⁶

2. Organized porous structures in soft lithography

Here, we demonstrate examples of utilization of microporous structures as complex masters for microprinting. Fig. 1a shows the schematic of the fabrication process which involves the preparation of the negative PDMS replica, followed by the infiltration of polystyrene (PS) solution into the receding portions of PDMS and finally, transferring and depositing the PS structure onto a different substrate. Capillary transfer lithography (CTL)⁵⁷ was chosen to reproduce a square array of air cylinders formed by interference lithography in SU8 material. A mixture of pre-polymer and curing agent (10:1) was poured onto the 2D structure, followed by degassing and curing at 75 °C. Subsequently, the PDMS was peeled from the SU8 to create a negative replica of the 2D organized porous structure of the initial architecture.

It is important to note that due to the high viscosity of the pre-polymer, only a partial infiltration (200 nm deep) into the SU8 porous structure is achieved. Complete infiltration of the viscous DMS into the pores requires external forces such as evacuation of the pores from the bottom. Despite these issues, it is interesting to note that the PDMS replica was extremely uniform over a large surface area as shown by the optical image (Fig. 1(b)). The inset FFT diagram shows the sharp spots originating from the highly ordered square lattice of the

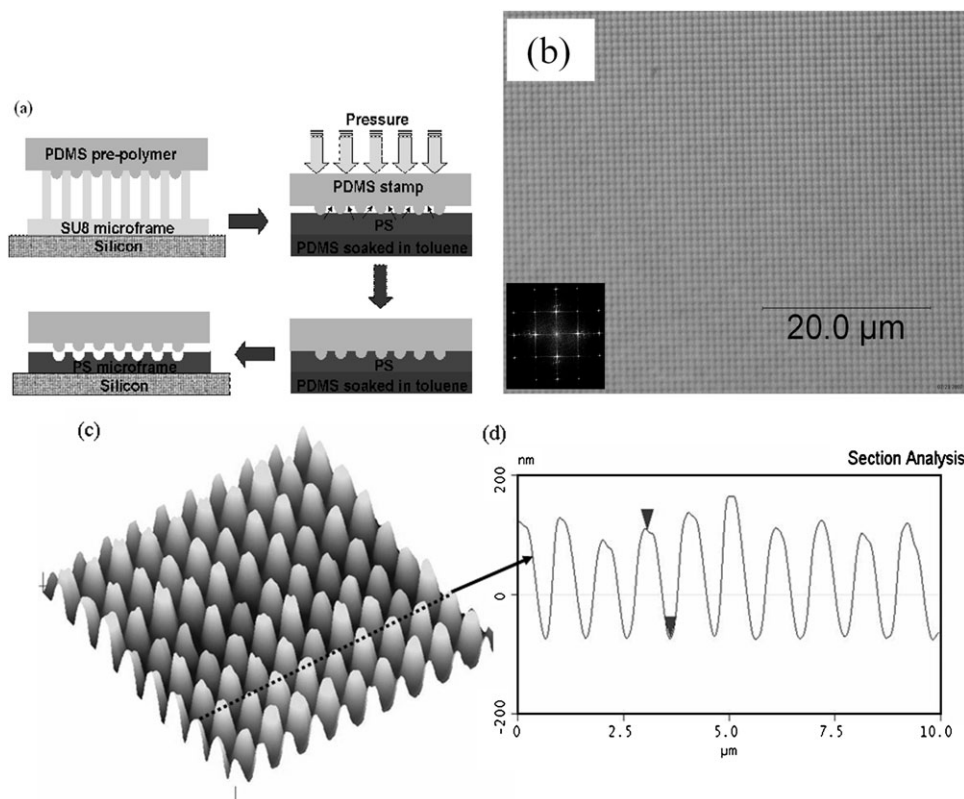


Fig. 1 (a) Schematic representation of the capillary transfer lithography using IL structures as masters; (b) Optical image of the PDMS stamp showing the large scale uniformity; (c) AFM image depicting the vertical posts (negative replica of SU8 master) of uniform height; (d) Cross section of AFM image showing the uniform height of the posts along the line shown in (c).

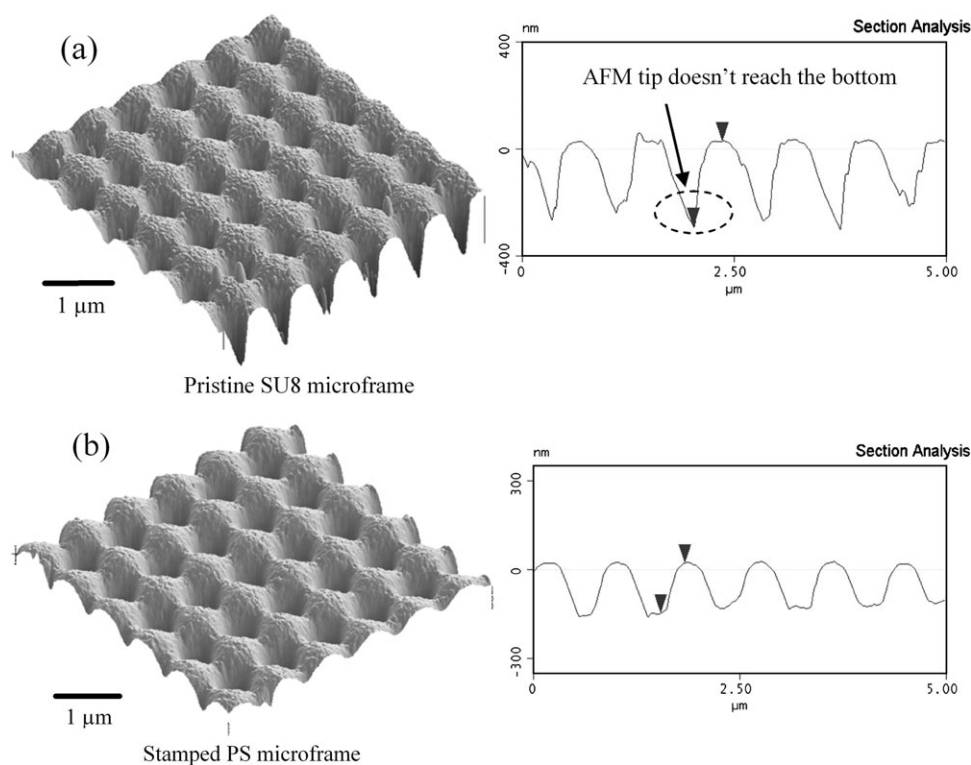


Fig. 2 AFM images and the corresponding cross sections of (a) pristine SU8 structure and (b) stamped PS structure showing identical topographical features down to the nanoscale.

arrays of vertical posts fabricated with this approach. Moreover, AFM image (Fig. 1(c)) shows a very uniform height of the vertical posts and the cross section of a post row shows the height to be nearly 200 nm for most of these posts.

In turn, these negative replicas can be used for the fabrication of organized structures from other polymers (Fig. 2). Fig. 2a and b show the AFM images and the corresponding cross sections of the original SU8 lattice along with the polystyrene (PS) stamped replica of SU8 square lattice structure. One can observe the remarkable similarity between the two structures with excellent replication of surface topology of the original SU8 periodic structure. In fact, even the nanoscale grainy morphology of the SU8 surface caused by non-uniform photopolymerization during the IL process was faithfully reproduced in the final structure.⁵⁸ It is worth mentioning that the PS stamped structures showed a significantly smaller vertical height (150 nm), measured from the AFM cross sections, as compared to that of PDMS posts (200 nm) due to the elastic deformation of the PDMS stamp during compression.

3. Mechanical properties of organized porous IL structures

The study of the small and large mechanical deformations of the organized porous structures presented here is important for understanding their behavior. On the other hand, this is a challenging task considering the dimensions of specimens (several micron thickness) and their attachment to the buffer surface layer. Both local elastic deformations of the nanoscale

features as well as the overall plastic behavior of the whole porous microstructure at large strains and ultimate failure are discussed in this section.

3.1 AFM nanomechanical measurements

AFM nanomechanical measurements are conducted to address the spatial distribution of the surface stiffness and the elastic response in the porous microstructure in accordance with the procedure adapted in our labs.^{59–61} Nanomechanical measurements were conducted in the elastic regime, with a small indentation depth allowing full elastic recovery of the probed areas as presented in our recent paper.⁶² The array of force–distance data obtained with surface force spectroscopy was converted to loading curves (indentation *vs.* load) to evaluate the surface stiffness and the elastic modulus for IL structures (Fig. 3). The Hertzian model of elastic deformation with correction on adhesive forces was applied by utilizing a semispherical indenter interacting with a planar elastic solid. This approximation is acceptable for the small penetration depths and intermediate loading rates as was discussed earlier.⁵⁹ Under these probing conditions, the viscoelastic contributions are negligible, as has been demonstrated in our previous publications.^{63,64}

Nanomechanical measurements of the pristine 2D porous SU8 structures conducted with a nanoscale indentation depth showed a clear bimodal distribution of the elastic response (shown in Fig. 3).⁶² A broad overall distribution of the elastic modulus ranging from 300 MPa to 1.7 GPa is due to local variations of the properties at nodes, struts, sidewalls, and slope regions (various regions shown in Fig. 3a). A statistically

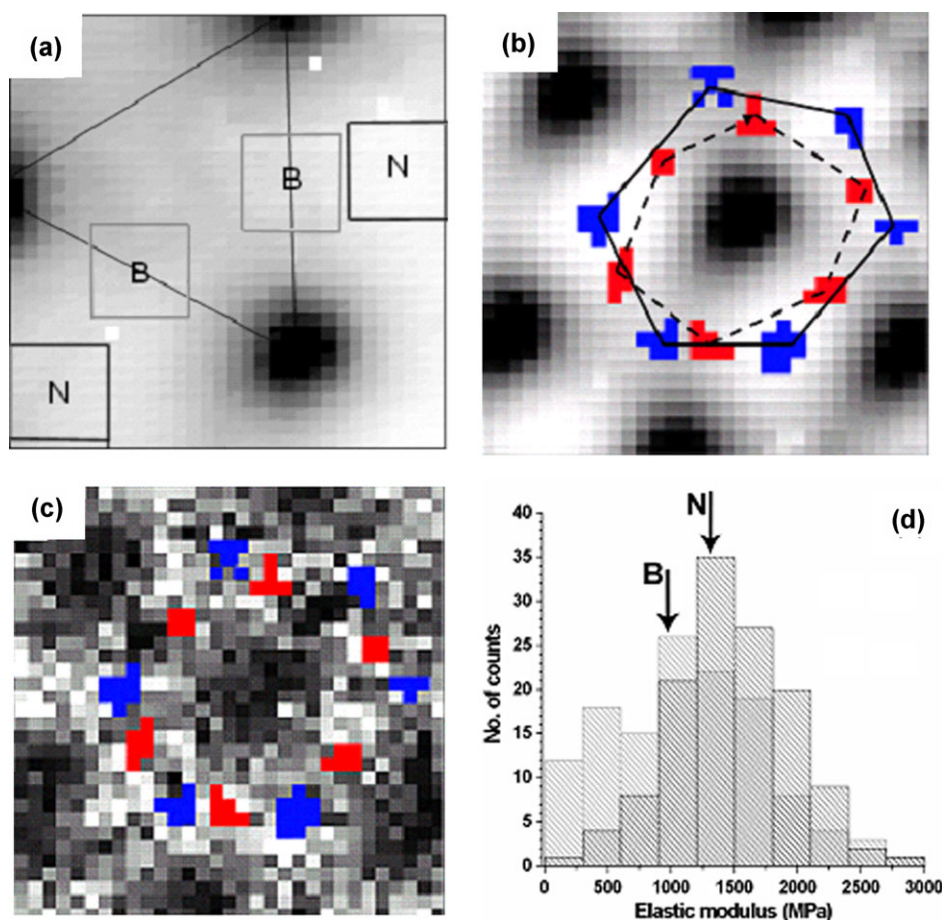


Fig. 3 (a) AFM topographic image of the 2D hexagonal lattice identifying the nodes (N) and beams (B) (b) 32×32 topography and (c) elastic modulus collected during force micromapping of the $2.5 \times 2.5 \mu\text{m}^2$ surface area (two designated areas are marked by squares of pixels (blue for nodes (N) and red for beams (B))); (d) combined surface histograms collected for selected surface areas ($500 \times 500 \text{ nm}^2$) for nodes (black boxes) and beams (gray boxes) (reprinted from ref. 62).

significant difference of the elastic modulus between nodes and beams was confirmed by the high resolution mapping of surface elastic properties (a single pixel of about 15 nm) (Fig. 3b and c). The average elastic modulus obtained from these histograms (Fig. 3d) for the nodes was 1480 MPa, which is higher than the calculated value for the beam areas (1120 MPa) due to periodic variation of the light intensity in the course of fabrication. Such a spatial variation is, probably, a very common feature which should be expected for any microstructure fabricated by interference lithography with continuously variable light intensity and thus continuously variable crosslinking density.⁶²

3.2 Large strain tensile measurements

However, highly localized AFM nanomechanical measurements provide little insight into the mechanical behavior at a macroscopic scale and for large deformations, which are relevant to the integrated mechanical applications. Therefore, microtensile tests were designed and performed on a 2D square lattice SU8 sample of 2 μm thickness with pores of 380 nm in diameter and with a spacing of 830 nm with effective porosity close to 20% (see Fig. 2a for surface topography).

Freestanding samples ($0.9 \text{ cm} \times 0.3 \text{ cm} \times 2 \mu\text{m}$) were mounted onto standard microtensile sample holders. Tensile measurements were performed with a force resolution of 3.5 mN and at a strain rate of 10^{-3} s^{-1} .

Fig. 4a and b show a stress and strain plot obtained under uniaxial tensile loading. The shaded area on this plot indicates continuous elastic resistance. Several spikes correspond to the formation of straight transversal cracks formed by gradual fracturing of the struts (Fig. 4c and d). The crack formation might be preceded by a local necking of the struts (Fig. 4d). However, the unperturbed regions still remain in the elastic regime as can be seen by the elastic response following the spikes. Sharp and multiple yield points correspond to the initiation and propagation of straight microcracks perpendicular to the stress direction (see representative cracks in Fig. 4c and d). Each straight crack causes the number of load bearing struts to decrease, which in turn lowers the effective modulus of the whole microstructure (see changes in slope in Fig. 4b). Such an unusual, stepwise mechanical deformation and fracturing is caused by a highly organized porous microstructure with a square lattice and only a few cracks required for sample fracturing. It is worth noting that similar load drops are observed in the polymer samples subjected to uniaxial and

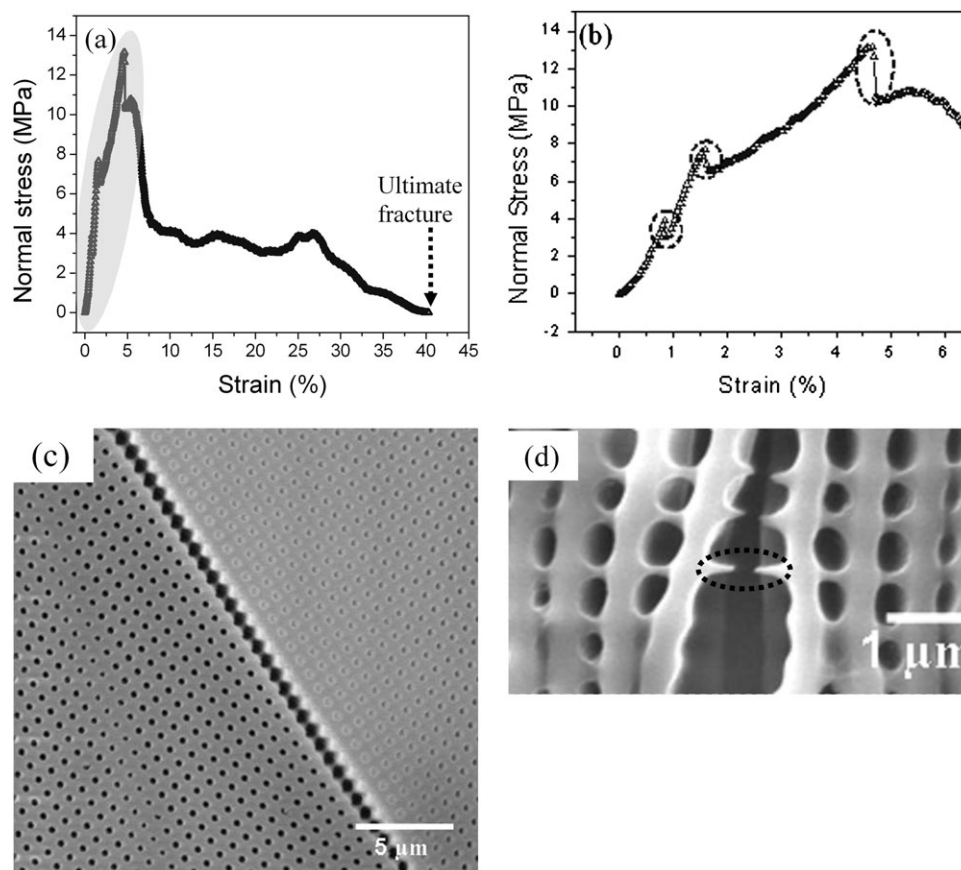


Fig. 4 (a) Stress–strain plot of tensile measurement performed on a 2D SU8 microframe, showing the multiple yield points followed by prolonged necking; (b) linear region of the stress–strain plot showing multiple yield points; (c) SEM image of the sample subjected to tensile measurement showing the crack propagation along [1 0] direction; (d) SEM image showing the necking and large plastic deformation of the struts.

high rate tensile strain due to initiation and localization of plastic deformation for highly inhomogeneous deformation at high strain rates (10^4 – 10^5 s $^{-1}$).⁶⁵ The stress–strain behavior shows an interesting effect: after the highest yield point (at 13 MPa), prolonged necking occurs before the ultimate failure.

Overall, the 2D square lattice structure exhibited remarkably high ultimate strain, reaching 35% which is very uncharacteristic behavior for homogeneous SU8 material with a high degree of crosslinking which is usually relatively brittle with small elongation to break (<5%).⁶⁶ Such large plastic deformation can be observed only for IL structures with very fine struts (Fig. 4d) with a diameter of several hundred nanometers and can be related to scale-controlled elasticity of modestly crosslinked elements of IL microstructures.⁵⁶ Such a prolonged necking of the fine struts under extended deformation provides extremely high toughness to these structures reaching high values of 1.5 MJ m $^{-3}$. The toughness of these structures measured here is nearly five times higher as compared to the random mats from drag line silk fibroin materials and layer-by-layer thin films, asserting the efficient energy absorption of the gradiently crosslinked SU8 microframe structures.^{67,68}

The elastic modulus of the 2D SU8 square lattice structure was calculated from the initial slope of the stress–strain curve to be 0.5 GPa. This value is much lower than that usually reported for the bulk SU8 material (2–4 GPa) and can be associated with porous architecture of these specimens

(Fig. 5(a)).⁶⁶ In fact, it is known that for cellular foam materials with a square lattice of air columns, the elastic modulus of the structure is anisotropic and is much lower than that for struts.²⁷ Indeed, the elastic modulus of the structure along [10] and [11] directions is given by $E_{[10]} = E_s (\frac{t}{l})^3$ and $E_{[11]} = 2E_s (\frac{t}{l})^3$ where E_s is the elastic modulus of the cell wall material, ‘ t ’ is the strut wall thickness, and ‘ l ’ is the distance between the adjacent struts (as schematically shown in Fig. 5b). For the 2D microframe investigated here, $t = 330$ nm, $l = 500$ nm and the elastic modulus of the SU8 material after IL fabrication is 1.1 GPa (see above). Thus, the effective elastic modulus of the microframe along [10] direction should be reduced to 0.7 GPa, which is close to the experimentally determined value of 0.5 GPa for the initial stage of the elastic stretching.

3.3 Fracture behavior of the organized porous structures

The ultimate performance of microframe structures can also be addressed using a simple peeling process that involves adhering an adhesive tape to the structure and peeling off a portion of the film from the substrate.⁶⁹ The remaining film is then transferred onto a carbon tape and mounted in an SEM holder. This peeling test involves a complex interplay of forces and allows us to observe the mechanical response of the microframe structure in a wide variety of deformational

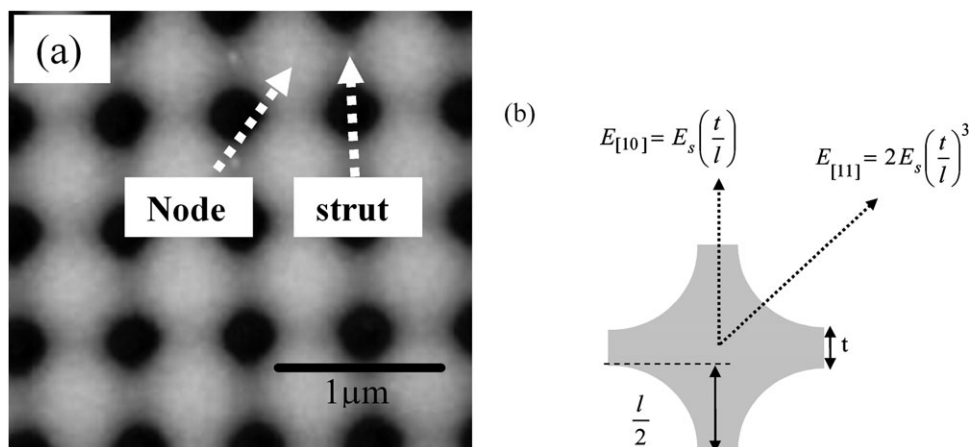


Fig. 5 (a) AFM image identifying the struts and the nodes of the 2D square lattice SU8 microframe; (b) schematic representation of unit cell of 2D square lattice and the elastic moduli in the two characteristic directions.

modes. We thus see the combined effect of tension, bending, compression, buckling, and shearing on our samples.

Inspection of the fractured film after this peeling procedure reveals a host of interesting deformed and fractured morphologies caused by various types of plastic deformations. Features associated with failure include long, straight, micrometer-wide cracks following particular lattice and easy-fracture directions, [10] and [01] directions in square lattice (see Fig. 6a). The lines of easy fracture always involve the failure of the thin, transversely oriented fine struts in the 2D lattice as has been discussed in detail in our recent paper.⁶⁹

Fig. 6b shows two other important modes of plastic deformation of the 2D sample under compression. The 2D microframe compressed laterally undergoes the collapse of the square lattice of cylindrical pores, forming a stack of thin wavy sheets. Furthermore, the stacks can undergo lateral compression in the perpendicular direction to the initial compressive forces resulting in correlated wrinkling in the plane of the lattice (Fig. 6c). Collapse of the struts and buckling of the thin walls are two efficient energy absorbing mechanisms playing a significant role in the deformation of these organized microstructures.

It is known that buckling of the cell walls in macroscopic cellular structures can occur in two distinct modes: creep buckling and catastrophic buckling.²⁷ Creep buckling of the wall involves the uniform sinusoidal deformation of structure, while catastrophic buckling involves acute curvature of the walls. Fig. 6b shows the uniform sinusoidal buckling of the thin wall structures which can be related to the creep buckling of the SU8 material. During the peel process, the microframe structure possibly undergoes lateral compression resulting in an in-plane periodic wrinkling pattern initiation. Upon further compression, the deformation of the lattice is localized within very short regions leading to a catastrophic buckling with sharp curvature. Such catastrophic buckling modes were observed in the fractured samples (Fig. 6c). It is important to note that various modes of deformation such as compression of the struts, sinusoidal buckling, and catastrophic buckling of the SU8 thin plates, are all plastic in nature. These large plastic deformations of the struts bridging the crack result in large

absorption of strain energy as observed in tensile measurements causing high toughness reaching 1.5 MJ m^{-3} (as was discussed above).

4. Bi-component organized IL structures

4.1 Infiltration of a second phase into open porous structures

Combining hard and soft polymer components (glassy-rubbery) provides advanced materials and coatings with synergistic properties and is frequently utilized for design of advanced polymeric composites.⁷⁰ For instance, a strong matrix serves as a load-bearing skeleton for structural integrity, while the soft component can be responsible for the adhesion control or for crack arresting. As is known, to achieve proper multiphase structure in conventional composite materials, a complex monitoring of the kinetics of phase separation of different components is required, as controlled by multiple processing stages (*e.g.*, adding a new component, temperature variation). Although a certain control of spatial scale, morphology, microstructure, and shape is achieved with temperature–composition variation, the resulting composites usually possess a high variation of feature dimensions, topology, and composition. These variations of structural parameters make it difficult to prevent a wide fluctuation of physical properties. While such a behavior affects the macroscopic properties of bulk composites to some extent, it can be much more critical for organized microstructural materials with overall dimensions (*e.g.*, thickness) comparable to the microphase domain dimensions (*e.g.*, polymer MEMS with sub-micron elements).

In view of the above consideration, we suggest that the organized porous IL structure can serve as an organized matrix for the fabrication of microcomposite materials with well-defined, uniform, and pre-determined spatial distribution of components or microphases. To implement this strategy, we have applied two independent approaches to infiltrate the second rubbery polymeric phase into the SU8 glassy microframe structure, namely, capillary driven infiltration of polymers and *in situ* polymerization in the microframe structure.

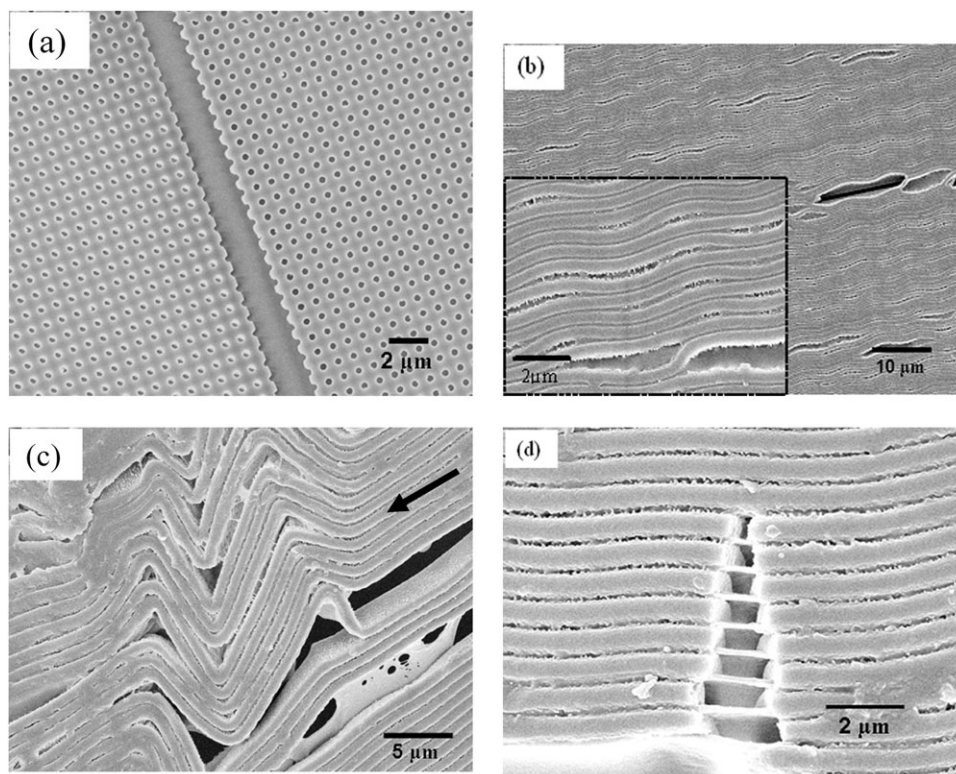


Fig. 6 SEM image showing fracture behavior of the 2D SU8 microframe: (a) fracture of 2D structure along the easy crack lines; (b) penny shaped cracks and sinusoidal buckling in the 2D microframe sample under compressive stress; (c) compressed regions of the microframe undergoing catastrophic buckling. Arrows indicate the direction of compression; (d) ultimate fracture of the compressed walls leading to the failure of the structure.

In the first method, capillary infiltration of the polymer was employed to fill the 2D open porous SU8 structure, as schematically represented in Fig. 7. The capillary force infiltration method uses capillary-driven filling of polymers softened by solvent (lowering the viscosity). The second polymer component (2% polybutadiene (PB) in toluene) is spin coated onto the PDMS substrate swollen in toluene. Swelling the substrate in toluene continuously supplies the solvent, softening the spin cast PB rubbery layer. Upon bringing the SU8

porous microstructure into intimate contact with the PDMS substrate, the PB solution fills the recessed region of the cylindrical pores (Fig. 7).

This method offers relatively uniform infiltration of the rubbery phase into the glassy polymer structure with cylindrical pores as illustrated by Fig. 8. One of the distinct advantages of the method is that it results in structures with pristine SU8 surface (with no residues of PB material on the SU8 surface). Fig. 8a and b show the AFM topography and phase images of the binary infiltrated structure, clearly depicting the distinct SU8 original structure (square matrix) and PB phase. The low surface energy of the PDMS substrate results in a poor interaction with PB, enabling the formation of

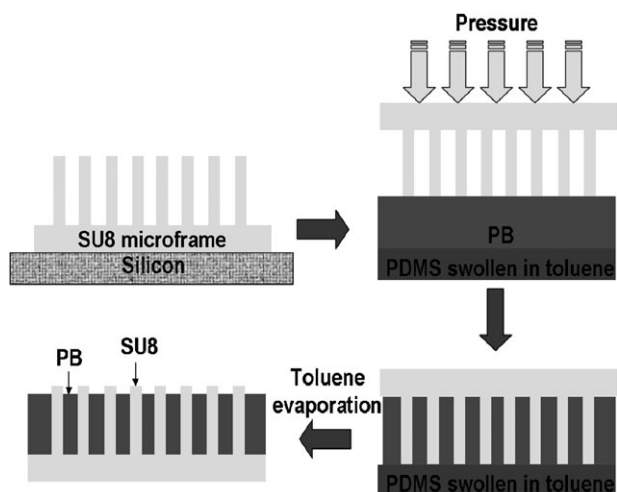


Fig. 7 Schematic representation of the capillary force assisted infiltration of PB solution into the SU8 porous structure.

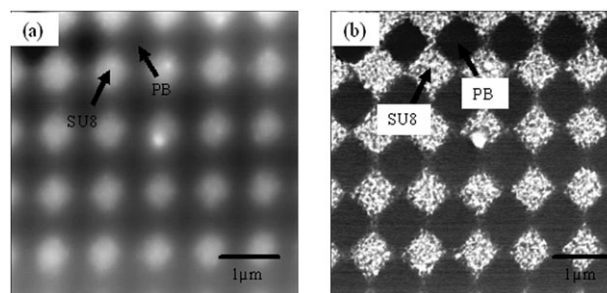


Fig. 8 AFM images depicting the SU8/PB bicomponent microstructure: (a) topography showing the uniform infiltration into the microframe (Z range: 100 nm); (b) phase image depicting the alternating bicomponent structure (phase scale: 50°).

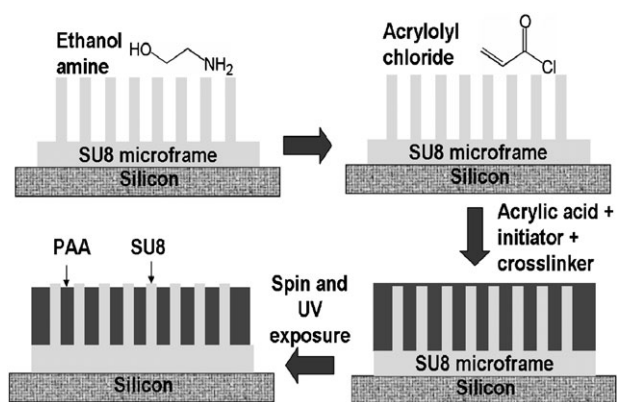


Fig. 9 (a) Schematic representation of the polymerization of acrylic acid solution in the pores of SU8 porous structure.

checkerboard PB-SU8 surface composition in the final structure.

The second method of the preparation of binary organized microcomposites involves the infiltration with acrylic acid (AA) monomer followed by UV-initiated photopolymerization (Fig. 9). This *in situ* photopolymerization of the acrylic acid results in a thin layer of PAA on the SU8 surface in addition to the holes being filled with crosslinked PAA material (Fig. 9). Prior to AA filling, pristine SU8 samples were treated with ethanol amine to reduce the hydrophobicity. The amine groups reacted with the uncrosslinked epoxy groups of the SU8, resulting in polar hydroxyl groups at the surface.⁷¹ Following the ethanol amine treatment (which resulted in a decrease in the contact angle

from 90 to 30°), the sample was thoroughly washed in Nanopure water and placed in a vial containing 1% acryloyl chloride in ethyl ether for 90 min. Then, the sample was washed thoroughly and immersed in a 20% acrylic acid solution with 5% UV initiator and 2% UV crosslinker (acryl amide), allowing the acrylic acid solution to infiltrate the pores. Finally, the sample was exposed to UV light (365 nm, 20 mW cm⁻²) to initiate the photopolymerization of acryl amide.

Fig. 10a shows the SEM image of the SU8 square lattice structure filled with PAA phase by the method described above. Fig. 10b shows the closer top view of the filled pores. Apparently, the PAA phase uniformly filled the cylindrical pores within SU8 structure uniformly over very large areas. Intentional fracture of the PAA-SU8 binary microcomposite film confirmed the complete filling of the pores (entire 2 μm thickness) with PAA material as can be seen on partially open pores (Fig. 10c). The PAA component was shaped by the SU8 porous lattice and was frequently found in the form of 2 μm long cylindrical flexible structures with 380 nm diameter which was occasionally pulled out during fracturing of the PAA-SU8 microcomposite material. It is worth to note that the polymerization of acrylic acid in the pores of the microframe structure and the subsequent solvent evaporation might result in significant compressive stress causing buckling in the periodic porous structure (Fig. 10d). Similar instabilities have been recently observed in macro and micro scale porous elastomeric structures subjected uniaxial and biaxial compressive stresses.^{55,72} The nature of the mechanical instabilities in periodic elastoplastic porous microstructures will be detailed in a separate publication.⁷³

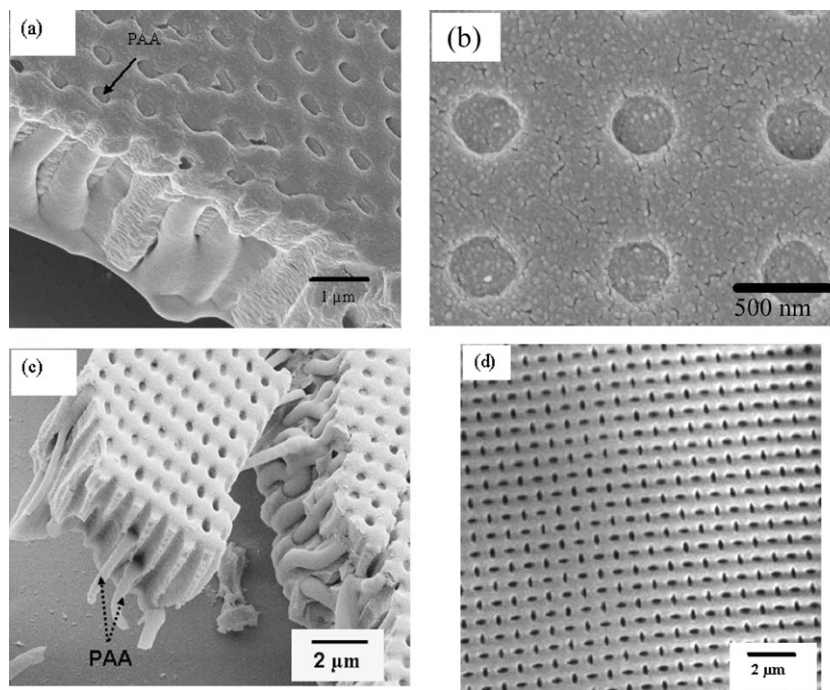


Fig. 10 SEM images of SU8 microframe with *in situ* polymerized acrylic acid: (a) angle view showing the PAA filling the pores of the SU8 microframe (inset shows the closer top view); (b) top view of filled pores at higher magnification; (c) side-view of the fractured sample showing the complete infiltration through the entire depth of the cylindrical holes and the pulled out cylindrical PAA domains; (d) top-view of herringbone pattern of SU8-PAA lattice caused by the collapse of the initial square lattice under compressive stresses during photopolymerization.

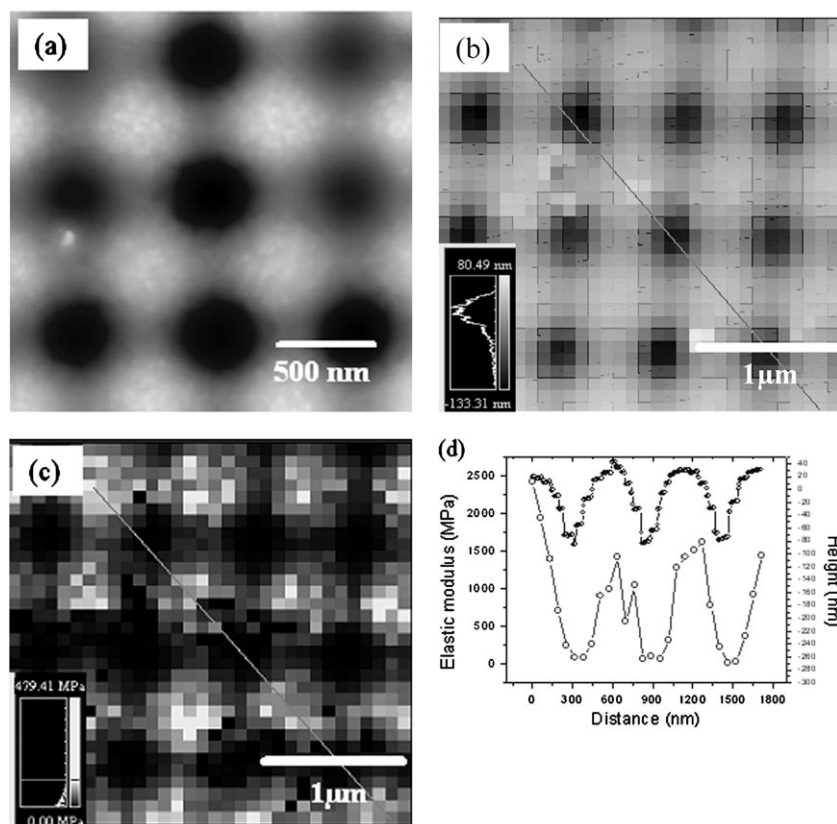


Fig. 11 (a) High resolution AFM topography image of the bicomponent microcomposite. AFM micromapping of the PB infiltrated SU8 square microframe: (b) 32×32 topography and (c) elastic modulus collected during force micromapping; (d) height (top) and elastic modulus (bottom) variation along cross section along the line shown in (b) and (c).

5. Mechanical behavior of bi-component ITL structures

5.1 AFM micromechanical measurements

AFM measurements on the SU8-PB binary microcomposites confirmed the templated periodic distribution of the glassy and rubbery microphases. Fig. 11a shows the high resolution AFM topographic image of the SU8-PB sample subjected to the AFM nanoindentation measurements. The height image of the SU8-PB structure confirms that the PB fills the pores with PB elevation remaining slightly below the SU8 template, as evident from the 80 nm height difference between the SU8 nodes and PB within pores. Although the polymer solution during the capillary process completely fills the pores, subsequent solvent evaporation causes the polymer to shrink inside the pores.

Fig. 11b and c show the height and the corresponding elastic modulus distribution of the bicomponent 2D microframe structure with glassy structure filled with a rubbery phase. The elastic modulus mapping shows that the SU8 regions possess much higher stiffness with an elastic modulus of 1200 ± 250 MPa, similar to that measured for the pristine SU8 structure (see histograms for different phases in Fig. 12). Contrarily, the PB-filled regions exhibit much lower elastic resistance with an elastic modulus of 12 ± 2 MPa, which is

close to that expected for conventional rubbery bulk PB material.⁷⁰ More detailed analysis with loading curves showed additional features.

Fig. 13a shows the mechanical load *vs.* penetration data obtained from three different regions on the SU8-PB microcomposite structure: SU8 surface (I), PB (III) microphase, and the interface between SU8 and PB (II) (see I, II, and III locations in Fig. 13c). From the loading data, it is clear that the rubbery PB regions (PB phase inside the pores) exhibit much higher elastic deformation compared to the interfacial regions, which in turn undergo higher deformation than that of the glassy material (compare penetration at identical loading forces in Fig. 13a). It is interesting to note that the initial portion of the indentation curve at interfacial location III (5 nm deformation) closely matches the pure PB phase and then exhibits a drastic change of slope indicating much higher resistance (Fig. 13b). This drastic change in the slope of the loading curve indicates that the AFM probe encounters underlying material with higher stiffness during the indentation process for the deformation beyond initial 10 nm.^{60,64}

In fact, the depth profile of the elastic modulus shown in Fig. 13b shows a gradual increase of the modulus with the indentation depth, which is a clear indication of the bilayered, rubber-glass structure along the edges of the pores. The regions along the circumference of the holes filled with PB exhibit an intermediate elastic modulus, ranging from the low

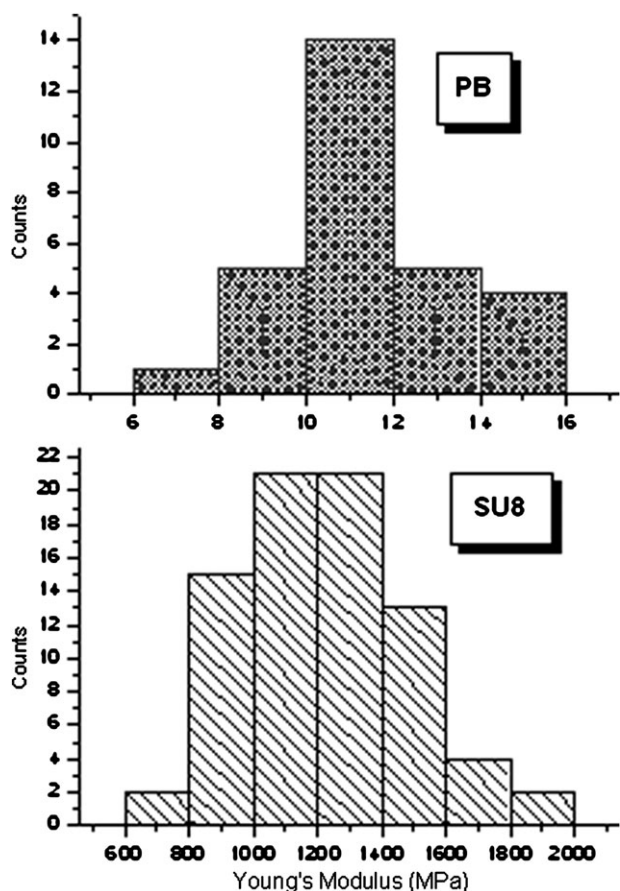


Fig. 12 Histograms showing the surface distribution of the elastic modulus in the SU8 and PB phases of the bi-component structure.

elastic modulus of PB (about 12 MPa) to a few hundred MPas (combined PB and SU8). This variation is caused by the interaction of the AFM tip with both materials in this transitions region with the presence of ultrathin (10 nm) surface PB layer covering SU8 material. Indeed, the concurrent cross section of the height and elastic modulus distribution (along the lines shown in Fig. 11a and b) demonstrated a gradual variation of the elastic response instead of abrupt transition across the pore rims (Fig. 11d). The presence of PB phase at the edges of the cylindrical pores resulted in the gradient of elastic modulus observed in this study and confirmed the general schematics of the distribution of glassy matrix and rubbery phase in the bicomponent SU8-PB microframe presented in Fig. 13c.

5.2 Fracture behavior of rubber-filled glassy IL structures

The peel test has been applied to study the fracture behavior of the PAA-SU8 binary microcomposite with 2D square symmetry. SEM images show the fractured areas of the PAA-SU8 sample exhibiting a fundamentally different deformation behavior compared to the original porous SU8 structure (Fig. 14). Both the SU8 struts and the PAA domains are stretched during the crack propagation, as can be seen in Fig. 14b. For these organized microcomposites, the cracks propagate *exclusively along* the [10] direction of the square lattice similar to that discussed above. However, unlike initial

porous structure, the rubbery microphases are stretched across the crack at very high elongation even after all SU8 struts of the matrix failed, thus, effectively bridging the opening at very high deformations (Fig. 14a). Rubbery PAA phase inside of cylindrical pores stretched across the crack openings exhibits significantly higher deformation (reaching 300–400%) compared to the SU8 struts (usually below 35% ultimate elongation). This way, the crack propagation is arrested by the stretched rubber microphases bridging across the SU8 edges, resembling the known crazing phenomenon in conventional rubber-toughened composite materials with ultimate toughness such as ABS plastics.⁷⁴

The unique feature of the organized PAA-SU8 structure is that the crack follows the selected lattice direction fracturing the PAA phase inside of cylindrical pores. This stretching of the PAA phase beyond failed struts should result in additional dissipation of strain energy at ultimate deformation conditions in a very different way as compared to conventional microcomposites. Indeed, in the case of the randomly distributed rubbery microphases, there are multiple random pathways in which the crack can propagate through glassy phase dissipating the least amount of mechanical energy and causing the macroscopic failure of the random microstructure. In contrast, for the organized bi-component rubbery-glassy structures discussed here, the crack's pathway through the rubbery-filled pores is predetermined by the matrix symmetry (square lattice in this case), which could possibly maximize energy dissipation during crack propagation. By directing the crack opening in the direction with maximized presence of the rubbery microphase inclusions.

It is worth to note that in the bicomponent microcomposites, we have primarily observed that the PAA domains stretch as opposed to the cavitation in the conventional composites.⁷⁰ The possible reason for the absence of cavitation in bicomponent microcomposites studied here might be the length-scale dependent mechanical properties of the SU8. It is known that one of the primary reasons for the cavitation of the rubber particles is the brittle nature of the surrounding matrix which facilitates significant difference in crack propagation velocities in glassy and rubbery regions. However, the IL crosslinked SU8 epoxy matrix can undergo significant plastic yielding (35% strain, as estimated from tensile test) before failure as opposed to the brittle fracture (<2% strain) in the case of the conventional highly crosslinked epoxy matrix. Moreover, in the case of the conventional rubber toughened composites, the rubber domains are separated by a few microns as opposed to the submicron separation in the case of the bicomponent microcomposite system (about 450 nm in our case). Thus the length scale dependent mechanical behavior of the matrix (microframe) might result in fundamentally different energy absorption mechanism in multicomponent organized microcomposites. Finally, it is important to note that the rubber domains stretching and bridging across the crack is an efficient energy absorption mechanism. Quantitative characterization of the toughness of the rubber filled microcomposites at different strain rates and with varying pore sizes is a subject of further investigation focused on understanding the energy dissipation characteristics in organized rubbery-glassy microcomposite materials.

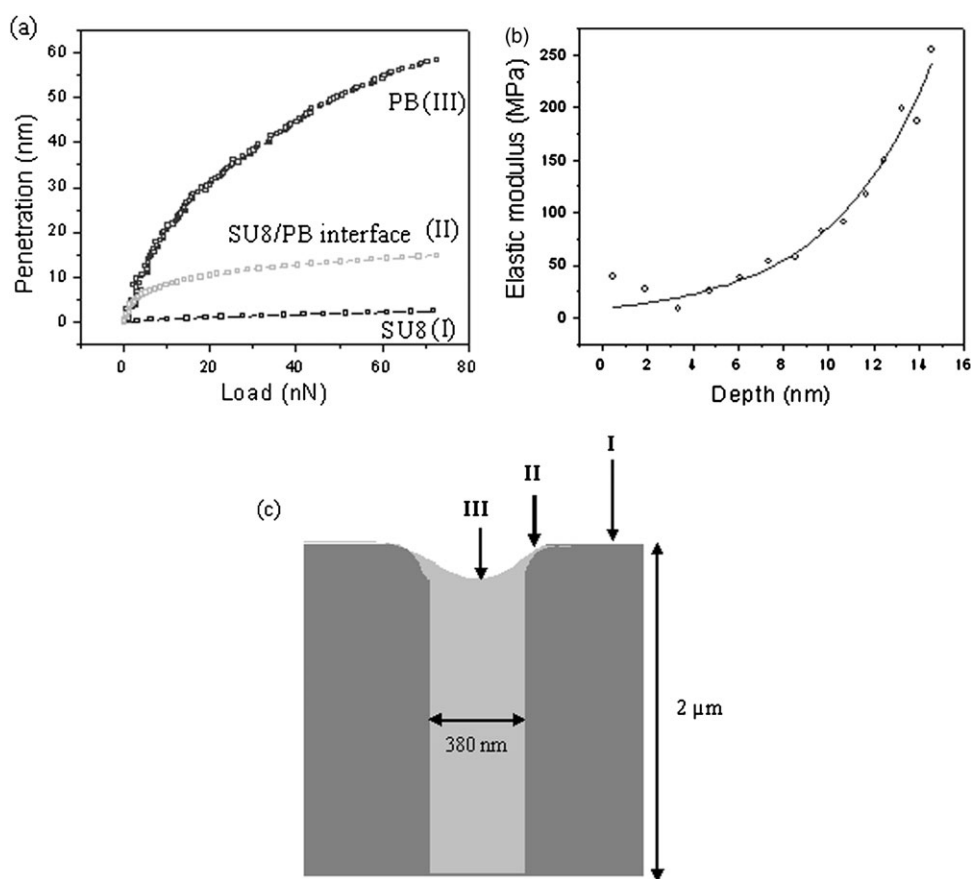


Fig. 13 (a) Representative loading curves from three different regions (SU8 (I), PB (III) and interface (II) as shown in (c)) of the bicomponent microcomposite; (b) depth profile of the elastic modulus at the interface of SU8 and PB (along the rim of the pore) showing the increasing elastic modulus with indentation depth; (c) the PB microphase in the SU8 pore showing the thin layer of PB on SU8 matrix along the circumference.

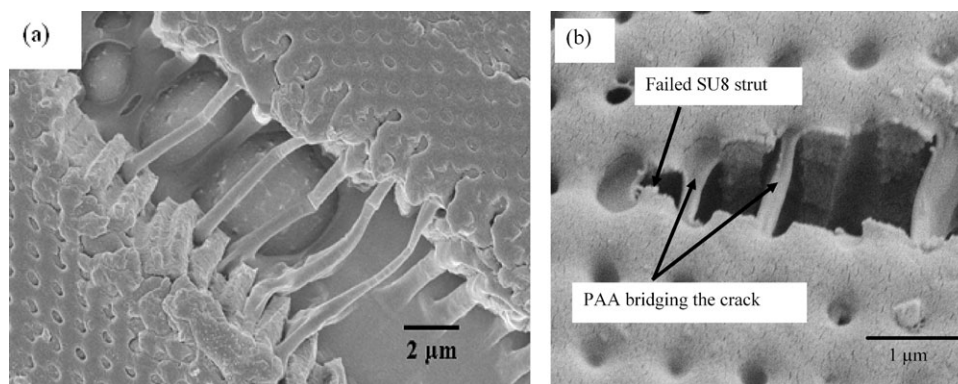


Fig. 14 SEM images showing the fracture in bicomponent SU8-PAA structures: (a) PAA inside the holes stretching ($\sim 300\%$) and forming fibrils across the crack; (b) Crack bisecting the rubbery PAA domains inside the porous matrix.

6. Conclusions

In conclusion, we have demonstrated that organized porous microstructures with continuous open microscopic pores obtained *via* interference lithography can be successfully utilized in the form of complex porous matrices for the fabrication of binary organized microcomposites with intriguing mechanical properties, such as lattice-controlled crack propagation, high toughness, and high energy dissipation due to multiple failures of struts and rubbery domains. Such organized glassy-rubbery

microcomposites fabricated with IL can find novel high-demanding applications, which require precise control of the mechanical elastic and plastic behavior at micro and nanoscale.

Acknowledgements

The work presented here is supported by NSF-CMS-0709586 and Institute for Soldier Nanotechnologies of the US Army

Research Office (under Contract DAAD-19-02-0002). The authors would like to thank Dr Melbourne LeMieux, Dr Taeyi Choi, Dr Chaitanya Ullal, for discussions and Prof. Satish Kumar, Dr Hyunhyub Ko, Dr Sergiy Peleshanko and Han Gi Chae for technical assistance.

References

1. Y. N. Xia, B. Gates, Y. D. Yin and Y. Lu, *Adv. Mater.*, 2000, **12**, 693.
2. P. T. Tanev, M. Chibwe and T. J. Pinnavaia, *Nature*, 1994, **368**, 321.
3. D. B. Akolekar, A. R. Hind and S. K. Bhargava, *J. Colloid Interface Sci.*, 1998, **199**, 92.
4. S. F. Xie, F. Svec and J. M. J. Frechet, *J. Chromatogr., A*, 1997, **775**, 65.
5. W. Busby, N. R. Cameron and C. A. B. Jahoda, *Polym. Interface*, 2002, **51**, 871.
6. T. Nishikawa, J. Nishida, R. Ookura, S. I. Nishimura, S. Wada and T. Karino, *Mater. Sci. Eng., C*, 1999, **8–9**, 495.
7. D. van Noort and C. F. Mandenius, *Biosens. Bioelectron.*, 2000, **15**, 203.
8. V. Malyarchuk, M. E. Stewart, R. G. Nuzzo and J. A. Rogers, *Appl. Phys. Lett.*, 2007, **90**, 203113.
9. *Micro- and Nanosystems: Information Storage and Processing Systems*, ed. B Bhushan, Springer, Berlin, Heidelberg, 2002.
10. *Microstructure and Microtribology of Polymer Surfaces*, ed. V. V. Tsukruk and K. Wahl, ACS Symposium Series, vol. 741, 2000.
11. I. Luzinov, S. Minko and V. V. Tsukruk, *Prog. Polym. Sci.*, 2004, **29**, 635.
12. C. Liu, *Adv. Mater.*, 2007, **19**, 3783.
13. H. Lorenz, M. Despont, N. Fahrni, N. LaBianca, P. Renaud and P. Vettiger, *J. Micromech. Microeng.*, 1997, **7**, 121.
14. N. T. Nguyen and T. Q. Truong, *Sens. Actuators, B*, 2004, **97**, 137.
15. V. Seidemann, S. Bütefisch and S. Büettgenbach, *Sens. Actuators, A*, 2002, **97**, 457.
16. H. Yu, O. Balogun, B. Li, T. W. Murray and X. Zhang, *J. Micromech. Microeng.*, 2004, **14**, 1576.
17. H. Lorenz, M. Laudon and P. Renaud, *Microelectron. Eng.*, 1998, **41**, 371.
18. R. G. Alargova, K. H. Bhatt, P. N. Paunov and O. D. Velev, *Adv. Mater.*, 2004, **16**, 1653.
19. S. Peleshanko, M. D. Julian, M. Ornatska, M. E. McConney, M. C. LeMieux, N. Chen, C. Tucker, Y. Yang, C. Liu, J. A. C. Humphrey and V. V. Tsukruk, *Adv. Mater.*, 2007, **19**, 2903.
20. M. Calleja, J. Tamayo, A. Johansson, P. Rasmussen, L. M. Lechuga and A. Boisen, *Sensor Lett.*, 2003, **1**, 20.
21. R. Bandorf, H. Lüthje, A. Wortmann, T. Staedler and R. Wittorf, *Surf. Coat. Technol.*, 2003, **174**, 461.
22. Y. Xia and G. M. Whitesides, *Angew. Chem., Int. Ed. Engl.*, 199, **37**, 550.
23. Y. Xia, J. A. Rogers, K. E. Paul and G. M. Whitesides, *Chem. Rev.*, 1999, **99**, 1823.
24. B. D. Gates, Q. Xu, J. C. Love, D. B. Wolfe and G. M. Whitesides, *Annu. Rev. Mater. Res.*, 2004, **34**, 339.
25. M. Ulbricht, *Polymer*, 2006, **47**, 2217.
26. D. Zimnitsky, V. V. Shevchenko and V. V. Tsukruk, *Langmuir*, 2008, DOI: 10.1021/la7038575.
27. L. J. Gibson and M. F. Ashby, *Cellular Solids Structure and Properties*, Cambridge University Press, Cambridge, 2nd edn, 1997.
28. V. S. Deshpande, N. A. Fleck and M. F. Ashby, *J. Mech. Phys. Solids*, 2001, **41**, 1747.
29. N. Wicks and J. W. Hutchinson, *Int. J. Solids Struct.*, 2001, **38**, 5165.
30. V. S. Deshpande, M. F. Ashby and N. A. Fleck, *Acta Mater.*, 2001, **49**, 1035.
31. A. G. Evans, J. W. Hutchinson, N. A. Fleck, M. F. Ashby and H. G. Wadley, *Progr. Mater. Sci.*, 2001, **46**, 309.
32. S. Yang, G. Chen, M. Megens, C. K. Ullal, Y. J. Han, R. Rapaport, E. L. Thomas and J. Aizenberg, *Adv. Mater.*, 2005, **17**, 435.
33. *Cellular Ceramics: Structure, Manufacturing, Properties and Applications*, ed. M Scheffler and P Colombo, Wiley, 2005.
34. S. Hyun, A. M. Karlsson, S. Torquato and A. G. Evans, *Int. J. Solids Struct.*, 2003, **40**, 6989.
35. O. D. Velev and E. W. Kaler, *Adv. Mater.*, 2000, **12**, 531.
36. M. L. Kai Hoa, M. Lu and Y. Zhang, *Adv. Colloid Interface Sci.*, 2006, **121**, 9.
37. M. E. Leunissen, *Nature*, 2005, **437**, 235.
38. E. V. Shevchenko, J. Kortright, D. V. Talapin, S. Aloni and A. P. Alivisatos, *Adv. Mater.*, 2007, **19**, 4183.
39. S. A. Davis, S. L. Burkett, N. H. Mendelson and S. Mann, *Nature*, 1997, **385**, 420.
40. G. Cook, P. L. Timms and C. G. Spickermann, *Angew. Chem., Int. Ed.*, 2003, **42**, 557.
41. Y.-H. Ha, R. A. Vaia, W. F. Lynn, J. P. Costantino, J. Shin, A. B. Smith, P. T. Matsudaira and E. L. Thomas, *Adv. Mater.*, 2004, **16**, 1091.
42. J. Y. Huang, X. D. Wang and Z. L. Wang, *Nano Lett.*, 2006, **6**, 2325.
43. M. Srinivasarao, D. Collings, A. Philips and S. Patel, *Science*, 2001, **292**, 79.
44. V. Z.-H. Chan, J. Hoffman, V. Y. Lee, H. Iatrou, A. Avgeropoulos, N. Hadjichristidis, R. D. Miller and E. L. Thomas, *Science*, 1999, **286**, 1716.
45. J.-H. Jang, C. K. Ullal, M. Maldovan, T. Gorishnyy, S. Kooi, C. Koh and E. L. Thomas, *Adv. Funct. Mater.*, 2007, **17**, 3027.
46. J. H. Moon, J. Ford and S. Yang, *Polym. Adv. Technol.*, 2006, **17**, 83.
47. J. H. Moon and S. Yang, *J. Macromol. Sci., Polym. Rev.*, 2005, **C45**, 351.
48. M. Maldovan, C. K. Ullal, W. C. Carter and E. L. Thomas, *Nat. Mater.*, 2003, **2**, 664.
49. C. K. Ullal, M. Maldovan, G. Chen, Y. Han, S. Yang and E. L. Thomas, *Appl. Phys. Lett.*, 2004, **84**, 5434.
50. D. Mei, B. Cheng, W. Hu, Z. Li and D. Zhang, *Opt. Lett.*, 1995, **20**, 429.
51. M. Campbell, D. N. Sharp, M. T. Harrison, R. G. Denning and A. J. Turberfield, *Nature*, 2000, **404**, 53.
52. S. Yang, M. Megens, J. Aizenberg, P. Witzius, P. M. Chaikin and W. B. Russell, *Chem. Mater.*, 2002, **14**, 2831.
53. B. Wagner, H. J. Quenzer, W. Henke, W. Hoppe and W. Pilz, *Sens. Actuators, A*, 1995, **A46**, 89.
54. J.-H. Jang, C. K. Ullal, T. Gorishnyy, V. V. Tsukruk and E. L. Thomas, *Nano Lett.*, 2006, **6**, 740.
55. T. Mullin, S. Deschanel, K. Bertoldi and M. C. Boyce, *Phys. Rev. Lett.*, 2007, **99**, 084301.
56. J.-H. Jang, C. K. Ullal, M. Maldovan, T. Gorishnyy, S. Kooi, C. Koh and E. L. Thomas, *Adv. Funct. Mater.*, 2007, **17**, 3027.
57. H. Ko, C. Jiang and V. V. Tsukruk, *Chem. Mater.*, 2005, **17**, 5489.
58. F. Hua, Y. Sun, A. Gaur, M. A. Meitl, L. Bilhaut, L. Rotkina, J. Wang, P. Geil, M. Shim and J. A. Rogers, *Nano Lett.*, 2004, **4**, 2467.
59. V. V. Tsukruk, Z. Huang, S. A. Chizhik and V. V. Gorbunov, *J. Mater. Sci.*, 1998, **33**, 4905.
60. H. Shulha, A. Kovalev, N. Myshkin and V. V. Tsukruk, *Eur. Polym. J.*, 2004, **40**, 949.
61. V. V. Tsukruk and Z. Huang, *Polymer*, 2000, **41**, 5541.
62. T. Choi, J.-H. Jang, C. K. Ullal, M. C. Lemieux, V. V. Tsukruk and E. L. Thomas, *Adv. Funct. Mater.*, 2006, **16**, 1324.
63. V. V. Tsukruk, V. V. Gorbunov, Z. Huang and S. A. Chizhik, *Polym. Int.*, 2000, **49**, 441.
64. A. Kovalev, H. Shulha, M. LeMieux, N. Myshkin and V. V. Tsukruk, *J. Mater. Res.*, 2004, **19**, 716.
65. S. Sarva, A. D. Mulliken and M. C. Boyce, *J. Phys. IV*, 2006, **134**, 95.
66. R. Feng and R. J. Farris, *J. Mater. Sci.*, 2002, **37**, 4793.
67. R. V. Lewis, *Chem. Rev.*, 2006, **106**, 3762.
68. C. Jiang, X. Wang, R. Gunawidjaja, Y.-H. Lin, M. K. Gupta, D. L. Kaplan, R. R. Naik and V. V. Tsukruk, *Adv. Funct. Mater.*, 2007, **17**, 2229.
69. J.-H. Jang, C. K. Ullal, T. Choi, M. C. Lemieux, V. V. Tsukruk and E. L. Thomas, *Adv. Mater.*, 2006, **18**, 2123.
70. L. H. Sperling, *Polymeric Multicomponent Materials*, John Wiley & Sons, Inc., New York, 1997.
71. M. Nordström, R. Marie, M. Calleja and A. Boisen, *J. Micromech. Microeng.*, 2004, **14**, 1614.
72. Y. Zhang, E. A. Matsumoto, A. Peter, P.-C. Lin, R. D. Kamien and S. Yang, *Nano Lett.*, 2008, **8**, 1192.
73. S. Singamaneni, K. Bertoldi, S. Chang, J.-H. Jang, E. L. Thomas, M. Boyce and V. V. Tsukruk, *Nat. Mater.*, submitted.
74. A. S. Argon, R. E. Cohen, O. S. Gebizlioglu and C. E. Schwier, *Adv. Polym. Sci.*, 1983, **52–3**, 275.